1-27-2020

Resolving the puzzle of single-atom silver dispersion on nanosized γ-Al2O3 surface for high catalytic performance

Fei Wang

Jinzhu Ma

Shaohui Xin

Qiang Wang

Jun Xu

See next page for additional authors

Authors
Fei Wang, Jinzhu Ma, Shaohui Xin, Qiang Wang, Jun Xu, Changbin Zhang, Hong He, and Xiao Cheng Zeng

nature COMMUNICATIONS

ARTICLE

https://doi.org/10.1038/s41467-019-13937-1 OPEN

Resolving the puzzle of single-atom silver dispersion on nanosized γ-Al_2O_3 surface for high catalytic performance

Fei Wang[1,2,6], Jinzhu Ma[1,2,3,6], Shaohui Xin[2,4], Qiang Wang[4], Jun Xu[4], Changbin Zhang[1,2*], Hong He[1,2,3] & Xiao Cheng Zeng[5*]

Ag/γ-Al_2O_3 is widely used for catalyzing various reactions, and its performance depends on the valence state, morphology and dispersion of Ag species. However, detailed anchoring mechanism of Ag species on γ-Al_2O_3 remains largely unknown. Herein, we reveal that the terminal hydroxyls on γ-Al_2O_3 are responsible for anchoring Ag species. The abundant terminal hydroxyls existed on nanosized γ-Al_2O_3 can lead to single-atom silver dispersion, thereby resulting in markedly enhanced performance than the Ag cluster on microsized γ-Al_2O_3. Density-functional-theory calculations confirm that Ag atom is mainly anchored by the terminal hydroxyls on (100) surface, forming a staple-like local structure with each Ag atom bonded with two or three terminal hydroxyls. Our finding resolves the puzzle on why the single-atom silver dispersion can be spontaneously achieved only on nanosized γ-Al_2O_3, but not on microsized γ-Al_2O_3. The obtained insight into the Ag species dispersion will benefit future design of more efficient supported Ag catalysts.

[1] State Key Joint Laboratory of Environment Simulation and Pollution Control, Research Center for Eco-Environmental Sciences, Chinese Academy of Sciences, Beijing 100085, China. [2] University of Chinese Academy of Sciences, Beijing 100049, China. [3] Center for Excellence in Regional Atmospheric Environment, Institute of Urban Environment, Chinese Academy of Sciences, Xiamen 361021, China. [4] State Key Laboratory of Magnetic Resonance and Atomic and Molecular Physics, Wuhan Institute of Physics and Mathematics, Chinese Academy of Sciences, Wuhan 430071, China. [5] Department of Chemistry, Department of Chemical & Biomolecular Engineering, and Department of Mechanical & Materials Engineering, University of Nebraska-Lincoln, Lincoln, NE 68588, USA. [6] These authors contributed equally: Fei Wang, Jinzhu Ma. *email: cbzhang@rcees.ac.cn; xzeng1@unl.edu

Alumina-supported silver (Ag/Al_2O_3) is a widely used catalyst in a variety of industrial applications, such as NO_x emission control via selective catalytic reduction (SCR) with using hydrocarbons (HC-SCR)[1–6] or NH_3 (NH_3-SCR)[7,8], soot oxidation[9,10], selective catalytic oxidation of ammonia (NH_3–SCO)[11–13], oxidation of volatile organic compounds[14,15], ethylene epoxidation[16,17], among others. The valence state, dispersion, and morphology of Ag species have been found to play important roles to the activities of Ag-based catalysts as these factors are all closely related to how Ag species are anchored on the Al_2O_3 surface. Hence, it is of both fundamental and technical importance to uncover the anchoring mechanism of Ag species on Al_2O_3 for the design of more efficient Ag/Al_2O_3 catalysts.

The strong metal–support interaction has been often identified as a key factor to affecting metal anchoring on oxide surfaces[18–20]. Both previous experiments[21] and DFT calculations[22] have shown that the presence of electronic defects on reducible oxides (e.g., CeO_2 and TiO_2) is the direct cause for the strong interaction between metal and support[19,23]. Due to the lack of electronic defects on nonreducible oxides such as Al_2O_3 and SiO_2, some other factors must be responsible for the dispersion and thermal stability of active metals. Kwak et al.[23] reported that unsaturated penta-coordinate Al^{3+} (Al^{3+}_{penta}) centers on the γ-Al_2O_3 surface, created by dehydration and dehydroxylation at 573 K, are the anchoring sites for Pt to entail strong interactions with γ-Al_2O_3 through oxygen bridges. They proposed that the coordinative saturation of Al^{3+}_{penta} sites is the driving force for Pt anchoring on γ-Al_2O_3. However, the source of the oxygen bridges was not explained specifically. Surface OH groups have also been shown to influence the dispersion of active metals on support (η-Al_2O_3 and SiO_2)[24,25], while the interaction between metals and OH groups has not been elucidated at the atomic level. Despite Ag/γ-Al_2O_3 catalysts have been extensively investigated, particularly on their valence state, dispersion, or morphology of Ag species, detailed anchoring mechanism of the Ag species on γ-Al_2O_3 surface is still unclear to date. Hence, it is timely to explore whether the Al^{3+}_{penta} sites, OH groups, or other sites are responsible for anchoring Ag species on γ-Al_2O_3, as well as the associated chemical mechanism for single-atom Ag dispersion.

Here, we select two kinds of γ-Al_2O_3, nanosized γ-Al_2O_3 and microsized γ-Al_2O_3 (details given in Supplementary Information Methods), as the support for the preparation of Ag/Al_2O_3 catalysts. Most surprisingly, we observe that Ag can be atomically dispersed on the nanosized γ-Al_2O_3, whereas Ag mainly exits in the form of nanoclusters on the microsized γ-Al_2O_3. By using a series of surface-science measurements and Density-functional-theory (DFT) computation, we reveal that the terminal hydroxyl groups on γ-Al_2O_3 surface are responsible for anchoring the Ag species on γ-Al_2O_3. More importantly, we find that the presence of abundant terminal hydroxyl groups on the nanosized γ-Al_2O_3 leads to the single-atom dispersion of Ag species on the γ-Al_2O_3 surface. As expected, the Ag/Al_2O_3 with single-atom dispersion of Ag species demonstrates markedly higher performance than cluster-dispersion of Ag species for the SCR of NO (SCR-NO) reaction.

Results

Ag dispersion on nanosized γ-Al_2O_3 and microsized γ-Al_2O_3. Nanosized γ-Al_2O_3 (nano-Al_2O_3, average size: 10 nm) and microsized γ-Al_2O_3 (micro-Al_2O_3, average size: 5 μm) were employed as the supports for the preparation of Ag/Al_2O_3 catalysts. HAADF-STEM images were taken to reveal the Ag morphology and dispersion on Ag/nano-Al_2O_3 with different Ag loadings (1, 2, 4%) and 1% Ag/micro-Al_2O_3 (see Fig. 1). As shown in (Fig. 1a, b),

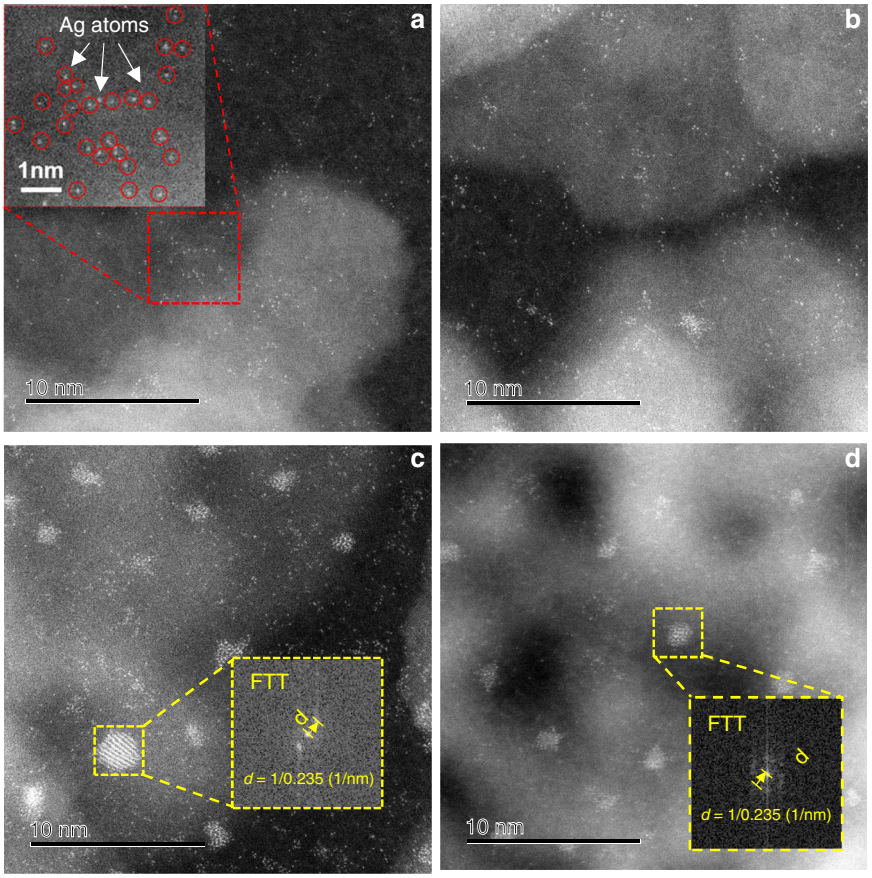

Fig. 1 HAADF-STEM images of Ag/γ-Al_2O_3 samples. a 1% Ag/nano-Al_2O_3, **b** 2% Ag/nano-Al_2O_3, **c** 4% Ag/nano-Al_2O_3 and **d** 1% Ag/micro-Al_2O_3.

atomically dispersed Ag species were observed for the 1% Ag/nano-Al_2O_3 sample, and Ag species still maintained atomic dispersion while a very few sub-nanometer Ag cluster species were also present on 2% Ag/nano-Al_2O_3. When the Ag loading was increased up to 4% (Fig. 1c), more Ag clusters appeared alongside Ag atoms, and the lattice spacing of Ag clusters was 0.235 nm, corresponding to the (111) planes of cubic metallic Ag (JCPDS file no. 01-071-3762)[26–28]. In contrast, as presented in Fig. 1d, single-atom Ag was rarely observed on 1% Ag/micro-Al_2O_3, while Ag nanoparticles of 2 nm average size (with lattice spacing = 0.235 nm) comprised the main morphology for Ag species. These results indicate that 1% Ag can be atomically dispersed on nano-Al_2O_3, whereas the Ag species agglomerates into nanoparticles on micro-Al_2O_3.

HC-SCR activity of Ag/Al_2O_3 with atomically dispersed Ag. Ag/Al_2O_3 catalysts have been extensively explored for the SCR of NO reaction, where both isolated Ag^+ species and $Ag_n^{\delta+}$ clusters are generally considered as the active centers[1,29–31]. We tested the 1% Ag/nano-Al_2O_3 and 1% Ag/micro-Al_2O_3 catalysts for C_3H_6-H_2-SCR and ethanol-SCR of NO to investigate the effect of Ag dispersion on catalytic activity. The results are shown in Fig. 2a, b, respectively. The 1% Ag/nano-Al_2O_3 presented much higher activity than 1% Ag/micro-Al_2O_3 for both C_3H_6-H_2-SCR and ethanol-SCR, demonstrating that the atomically dispersed Ag species on Ag/nano-Al_2O_3 are markedly superior to the Ag nanoparticles on Ag/micro-Al_2O_3. These results suggest that isolated Ag^+ species are more active than $Ag_n^{\delta+}$ clusters or Ag nanoparticles for NO_x reduction. After HC-SCR of NO testing, the morphology of single-atom dispersed Ag on 1% Ag/nano-Al_2O_3 catalyst was investigated again by using HAADF-STEM, and the images are shown in Fig. 2c, d. There was no sign of agglomeration of single-atom Ag species on spent Ag/nano-Al_2O_3 sample, indicating the single-atom dispersed Ag on the nano-Al_2O_3 catalyst was very stable.

Charge state of Ag species and its connection with γ-Al_2O_3. To solve the puzzle regarding the distinct dispersion behavior of Ag species on nano-Al_2O_3 and micro-Al_2O_3 sample, we first attempted to identify the anchoring site and the associated chemical mechanism for Ag species on γ-Al_2O_3. We noted that Kwak et al.[23] reported that Al^{3+}_{penta} centers on γ-Al_2O_3, created by dehydration and dehydroxylation at 573 K (see the diagram in Fig. 3d), are the anchoring sites for Pt, and that the coordinate saturation is the driving force due to the changes in NMR signal of Al^{3+}_{penta} centers after Pt loading. Hence, first, we examined the possibility of Ag anchoring on Al^{3+}_{penta} centers at room temperature by using ^{27}Al solid state MAS NMR. The NMR spectra of the nano-Al_2O_3 and 1% Ag/nano-Al_2O_3 samples were collected and the results are presented in Fig. 3a. No NMR signal of Al^{3+}_{penta} sites (at 35 ppm)[23] on pristine nano-Al_2O_3 was seen, and the Ag loading on nano-Al_2O_3 apparently induced little changes in the coordination number of Al. These results show that the nano-Al_2O_3 is coordinately saturated during the preparation of Ag/nano-Al_2O_3 without pre-dehydroxylation; therefore, Al^{3+}_{penta} centers are not the anchoring sites for Ag species, and there should be another site responsible for the Ag anchoring on γ-Al_2O_3 surface.

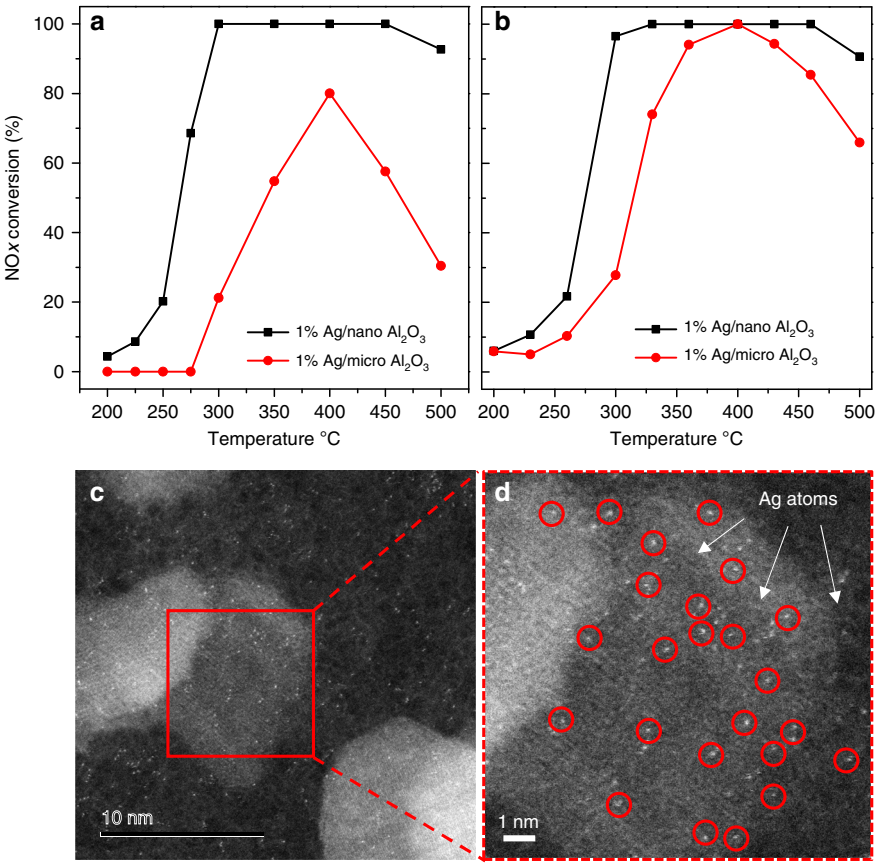

Fig. 2 HC-SCR activities of 1% Ag/γ-Al_2O_3 and HAADF-STEM images of 1% Ag/nano-Al_2O_3 after testing. NO_x conversion for **a** C_3H_6-H_2-SCR (NO 800 ppm, C_3H_6 1565 ppm, H_2 1%, O_2 10%, N_2 balance. GHSV 100,000 h^{-1}), **b** ethanol-SCR (NO 800 ppm, C_2H_5OH 1565 ppm, O_2 10%, H_2O 5%, N_2 balance. GHSV 100,000 h^{-1}) of NO over 1% Ag/nano-Al_2O_3 and 1% Ag/micro-Al_2O_3. **c**, **d** HAADF-STEM image and drawing of partial enlargement of 1% Ag/nano-Al_2O_3 after ethanol-SCR reaction.

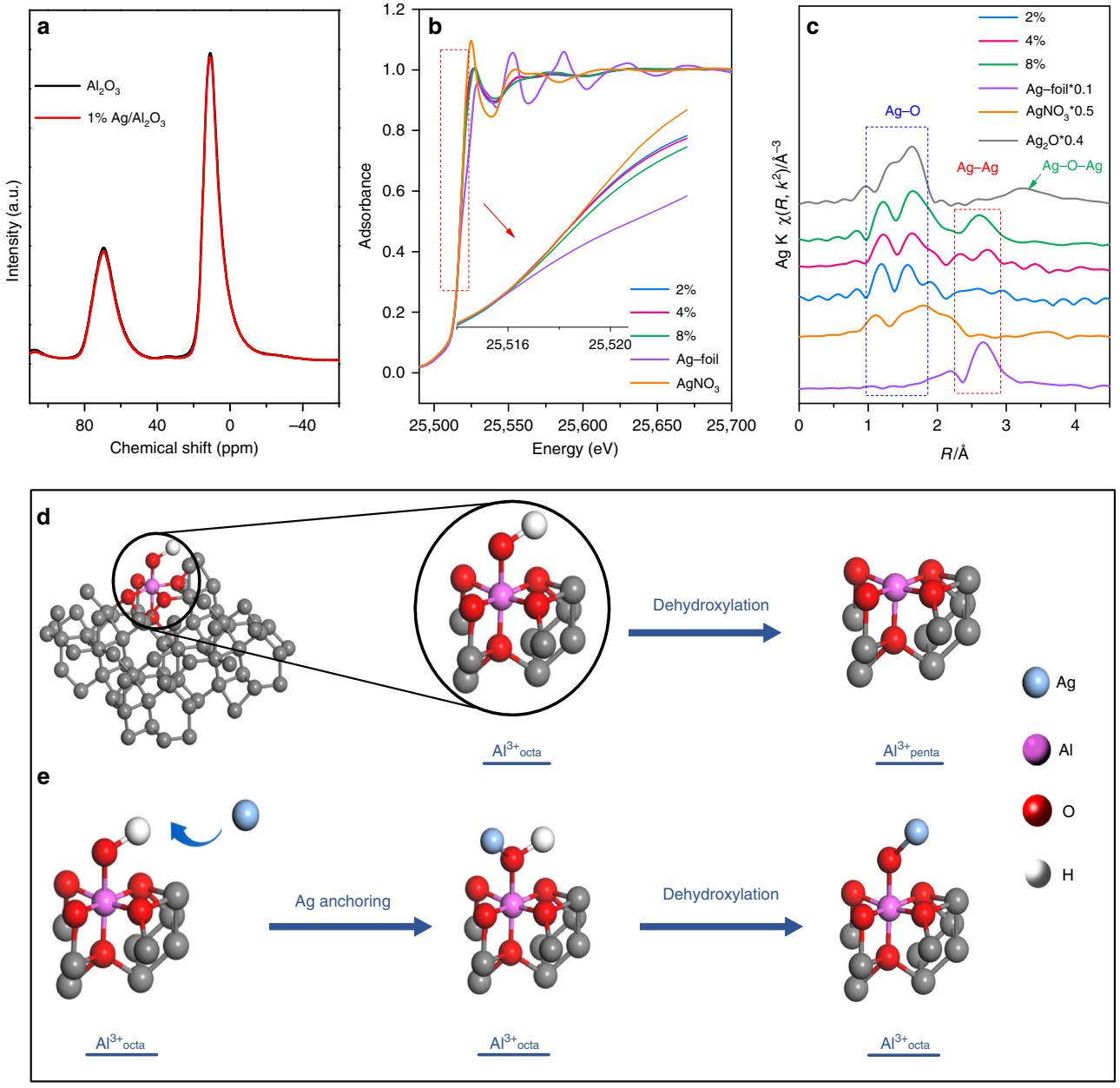

Fig. 3 ^{27}Al NMR and XAFS characterization of Ag/nano-Al_2O_3 and analysis of Ag anchoring. a Normalized ^{27}Al MAS NMR spectra of nano-Al_2O_3 and 1 wt% Ag/nano-Al_2O_3. **b**, **c** Ag-K edge XANES and EXAFS spectra of standard samples and Ag/nano-Al_2O_3 with different Ag loadings (2, 4, 8%) (Fourier transform *k* range 2.9-14.3 Å^{-1}). **d** A diagram showing possible formation process of Al^{3+}_{penta} from Al^{3+}_{octa} through dehydroxylation on Al_2O_3. **e** A diagram showing possible process of Ag anchoring through interaction between Ag and Al-OH.

XRD results of Ag/nano-Al_2O_3 with various Ag loadings (see Supplementary Fig. 1) show typical diffraction peaks of γ-Al_2O_3 (JCPDS 02-1420), while no Ag-containing phases appear until the Ag loading reaches 4 wt%, indicating that Ag species are in high dispersion at low loadings. Previously, we measured the UV–vis profiles of Ag/nano-Al_2O_3 and Ag/micro-Al_2O_3 with various Ag loadings[12]. The UV–vis spectra of 1% Ag/nano-Al_2O_3 and 1% Ag/micro-Al_2O_3 after the Kubelka–Munk transformation are presented in Supplementary Fig. 2a. The spectra were deconvoluted into Gaussian subbands on the basis of the assignments. Next, the percentages of Ag species were calculated based on an analysis of the integrated peak areas. As shown in Supplementary Fig. 2b, the percentage of isolated Ag^+ was more than 95% on nano-Al_2O_3, while about 60% of Ag species existed in the $Ag_n^{\delta+}$ state on micro-Al_2O_3. These UV–vis results reveal that the Ag species on nano-Al_2O_3 are mainly the isolated Ag^+ ions at low Ag loading (1–2 wt%) and form the metallic Ag_n clusters at relatively high Ag loading (4–8 wt%)[6,30,32–37], whereas even 1% Ag on micro-Al_2O_3 tends to form $Ag_n^{\delta+}$ clusters, consistent with the HAADF-STEM images. XAFS measurements were then conducted to study the valence and coordination condition of Ag species on the nano-Al_2O_3 surface. Ag-K edge X-ray adsorption spectra of Ag/nano-Al_2O_3 with different Ag loadings (2, 4, and 8 wt%) were measured, together with those of Ag foil, Ag_2O, and $AgNO_3$ as references. The normalized near-edge structure (XANES) of the samples (Fig. 3b) further shows that the Ag was in the oxidized state at low Ag loadings (2 wt%) and closer to the metallic state at high Ag loadings (4 and 8 wt%)[38,39]. Fourier transforms of k^2-weighted extended X-ray absorption fine structure (EXAFS) spectra of standard samples and Ag/nano-Al_2O_3 with different

Ag loadings (2, 4, and 8 wt%) are shown in Fig. 3c. The peak at about 1.7 Å was assigned to Ag–O interactions[40,41], and it exhibits similar peak intensities in the spectra of the three Ag/nano-Al_2O_3 samples. An intense peak at 2.67 Å also appeared when Ag loading was increased to 4 or 8%. This peak is similar to that of Ag foil, and was therefore attributed to Ag–Ag metallic bonding, indicating the formation of Ag clusters in the metallic state (Ag_n^0)[40,41]. In addition, no Ag–O–Ag shell was detected in any of the Ag/nano-Al_2O_3 samples.

These results above demonstrate that Ag species initially connect to Al_2O_3 through oxygen bridges during Ag loading, and then aggregate to form metallic Ag when the oxygen bridges are depleted with increasing the Ag loading. Hence, it is critical to find the origin of oxygen bridges in order to understand the Ag anchoring mechanism. All of Ag species are in ionic state during the impregnation step, therefore the oxygen bridge should be only originated from the γ-Al_2O_3 substrate. Surface oxygen atom generally exits in a form of hydroxyl groups, and it is known that γ-Al_2O_3 surface entails abundant and diverse surface hydroxyl groups. Since Ag^+ has high electron affinity[42], we speculated that Ag species are mainly anchored by the Al–OH sites through interaction between Ag^+ and O atoms. If so, the oxygen bridges would remain unchanged after the Ag loading (as schematically shown by the diagram in Fig. 3e).

Correlation between Ag loading and hydroxyl content. The relationship between hydroxyl content and Ag loading was investigated through the ^{1}H MAS NMR method and the results are displayed in Fig. 4a. The overlapping spectra were deconvoluted, and three peaks centered at −0.2, 1.3 and 4.0 ppm chemical shifts were fitted for the nano-Al_2O_3 support (zero Ag loading, 0% Ag). According to the literatures[43–46], the bands at −0.2 and 1.3 ppm were assigned to HO-μ^1 (Al_{IV}) and HO-μ^2 (Al_v, Al_n), respectively, and the broader band at 4.0 ppm was assigned to the HO-μ^3 (Al_n) and residual water [here, μ^1, μ^2, μ^3 represent terminal (type I), doubly bridging (type II), triply bridging (type III) hydroxyls]. Loading Ag onto the nano-Al_2O_3 induced a substantial reduction in the peak intensity of the terminal hydroxyl groups (−0.2 ppm), evidencing the sharp decrease in the number of hydroxyl groups with 1 or 2% Ag loading. In contrast, no obvious decrease in peak intensities was observed for doubly and triply bridging hydroxyls. These results show that the terminal hydroxyl groups on Al_2O_3 surface are responsible for anchoring the Ag species. In addition, a new peak at around 0.2 ppm arisen with the Ag-loaded samples, thereby being relevant to the Ag species. Thus, the new peak was tentatively assigned to a new type of doubly bridging hydroxyls [type II', HO-μ^2 (Ag, Al_n)], owing to the anchoring of Ag on terminal hydroxyl groups.

Surface OH groups on Al_2O_3 can act as acid sites, and NH_3 adsorption could take place on these sites. Therefore, monitoring the changes in OH-related peaks by FTIR during NH_3 adsorption can be used to characterize the types, strengths, and concentrations of surface OH groups. If Ag species occupy the OH sites when being loaded on γ-Al_2O_3, the intensities of negative OH peaks would decrease since fewer OH sites are available for NH_3 adsorption. In situ DRIFTS of NH_3 adsorption was then carried out on Ag/nano-Al_2O_3 samples to further study more detailed relationship between

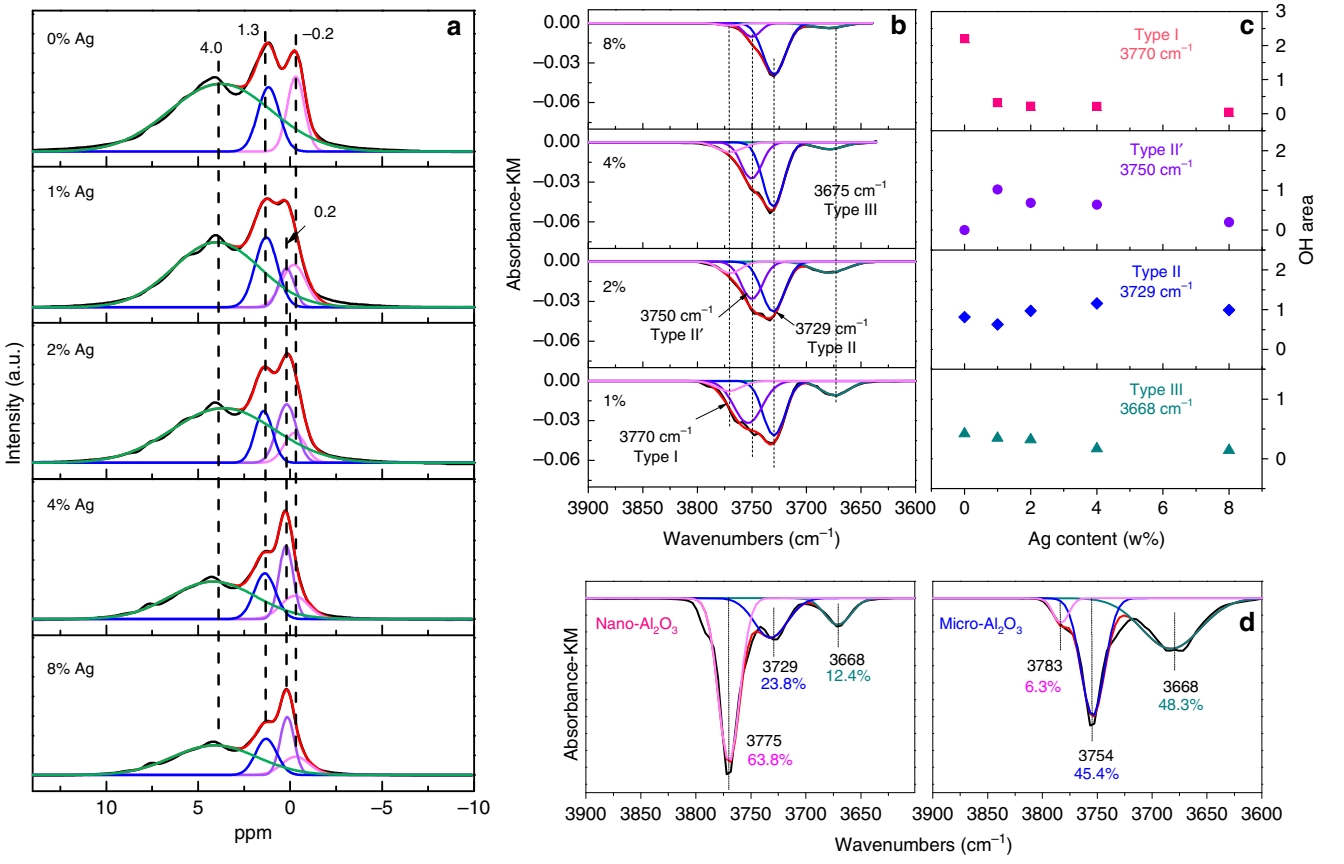

Fig. 4 ^{1}H NMR and in situ DRIFTS spectra of Ag/γ-Al_2O_3. **a** Normalized ^{1}H MAS NMR of Ag/nano-Al_2O_3 with different silver loadings (0, 1, 2, 4, 8%) (Samples were dehydrated at 473 K for 12 h before NMR measurements), **b** peak resolving of OH consumption peaks after in situ DRIFTS of NH_3 adsorption over Ag/nano-Al_2O_3 with different silver loadings (0, 1, 2, 4, 8%), **c** relationship between Ag content and peak areas of hydroxyl groups, **d** peak resolving of OH consumption peaks after in situ DRIFTS of NH_3 adsorption over nano-Al_2O_3 and micro-Al_2O_3.

Ag anchoring and surface hydroxyl groups (see Supplementary Fig. 3). The bands at 1689, 1478, and 1395 cm^{-1} were attributed to the vibrations of NH_4^+ chemisorbed on Brønsted acid sites[47–49]. The bands at 1614 and 1239 cm^{-1} were assigned to NH_3 on Lewis acid sites[49–51]. It is well established that γ-$A1_2O_3$ surfaces contain various types of OH groups, characterized by their O–H stretching frequencies. The negative bands at 3775, 3729, and 3668 cm^{-1} were assigned to the occupation of isolated hydroxyl group of type I, II, and III[52–60], respectively. The peak intensities for the surface OH groups[52,53] clearly decreased after Ag species were loaded, indicating that some OH sites were occupied by Ag species.

The overlapping peaks related to OH occupation over Ag/nano-Al_2O_3 with different silver loadings (0, 1, 2, 4, 8%) were deconvoluted (see Fig. 4b, d). Four subpeaks were assigned to three types of OH groups (type I, type II, type III) and the newly formed OH groups (type II′), respectively. The peak areas were calculated by integration, and the correlations between Ag content and hydroxyl peak areas were next analyzed. As shown in Fig. 4c, the peak area of terminal OH groups (type I) was sharply dropped at Ag loading of 1 and 2%, but further increasing the Ag content to 4 and 8% induced no obvious change in peak area. Meanwhile, a new type of doubly bridging OH groups (type II′) appeared at 3750 cm^{-1} after Ag was loaded. In contrast, there was no correlation between Ag loading and the other two types of OH groups (type II, III). These results strongly support that Ag species are anchored on the Al_2O_3 surface through interaction between Ag and terminal hydroxyl groups (type I), while producing a new type of hydroxyl group.

We also measured the concentration of surface OH groups on microsize Al_2O_3 using in situ DRIFTS spectra of NH_3 adsorption, and compared with those on nano-Al_2O_3. As shown in Fig. 4d, the content of terminal hydroxyl groups in micro-Al_2O_3 was only 6.3 %, about ten times lower than that in nano-Al_2O_3 (63.8%). Since the nano-Al_2O_3 contains abundant terminal hydroxyls for Ag anchoring, 1% Ag can be dispersed in single-atom Ag fashion on nano-Al_2O_3. In contrast, there are insufficient number of terminal hydroxyl groups on micro-Al_2O_3 for anchoring 1% Ag. As such, Ag species aggregate into Ag cluster on micro-Al_2O_3.

Anchoring mechanism of Ag on terminal hydroxyl groups. DFT calculations were carried out to investigate the interaction between Ag species and hydroxyl groups. Previous studies have shown that the (110) surface dominates on γ-Al_2O_3, which occupies about 70% of the total area, followed by the (100) surface (~20% of the total area)[57,61]. The relaxed structures of the dehydrated (100) and (110) surfaces of γ-Al_2O_3 were shown in Supplementary Fig. 4. A total of 16 Al atoms and 24 O atoms were exposed on (110) surfaces of 2 × 2 γ-Al_2O_3, where Al atoms were classified as Al_{trip} and Al_{tetra}, and O atoms were O_{two} and O_{trip}, respectively. A total of 16 Al atoms and 24 O atoms were also exposed on the (100) surfaces of 2 × 2 γ-Al_2O_3. However, Al atoms were Al_{tetra} and Al_{penta}, and O atoms were only O_{trip}, respectively. Since our catalysts were prepared by using the impregnation method in DI-water, the (100) and (110) surfaces of γ-Al_2O_3 in the calculation were considered to be 100% hydroxylated. The hydroxyl surface coverage of γ-Al_2O_3 (100) and (110) facet in this work is 16.5 OH nm^{-2} and 14.7 OH nm^{-2}, respectively. These results are within the range of OH surface coverage reported by Digne et al.[61]. We further calculated the stretching frequencies of the OH species on the (100) and (110) surfaces. The results are given in Supplementary Table 1. It is shown that the calculated frequencies are in good agreement with the data previously reported[61], and also in line with the assignment of the experimental values (Fig. 4b).

The hydroxylated (110) and (100) surfaces of γ-Al_2O_3 were then relaxed (see Fig. 5a). For the (110) surface, there are three types of hydroxyl groups (types I–III), and the fraction of terminal hydroxyl groups (type I) is ~30%. For the (100) surface, surface reconstruction occurs after hydroxylation, and all Al atoms become six-coordinated. So, only two types of hydroxyl groups (type I and type III) are present on the (100) surface, and the fraction of terminal hydroxyl groups (type I) is 52%. These results indicate that terminal hydroxyl groups (type I) are more easily formed on (100) surfaces of γ-Al_2O_3. XRD profiles (Supplementary Fig. 5) show that nano-γ-Al_2O_3 exhibited more (100) surfaces than micro-γ-Al_2O_3, supporting that nano-γ-Al_2O_3 entails much more terminal hydroxyl groups (type I) (see Fig. 4).

We then calculated the interaction between Ag atom and different types of hydroxyls on the (110) and (100) surfaces of γ-Al_2O_3. For the (110) surface, considering different coordination environments of hydroxyl groups, there are three types of terminal hydroxyls (type I), two types of doubly bridging

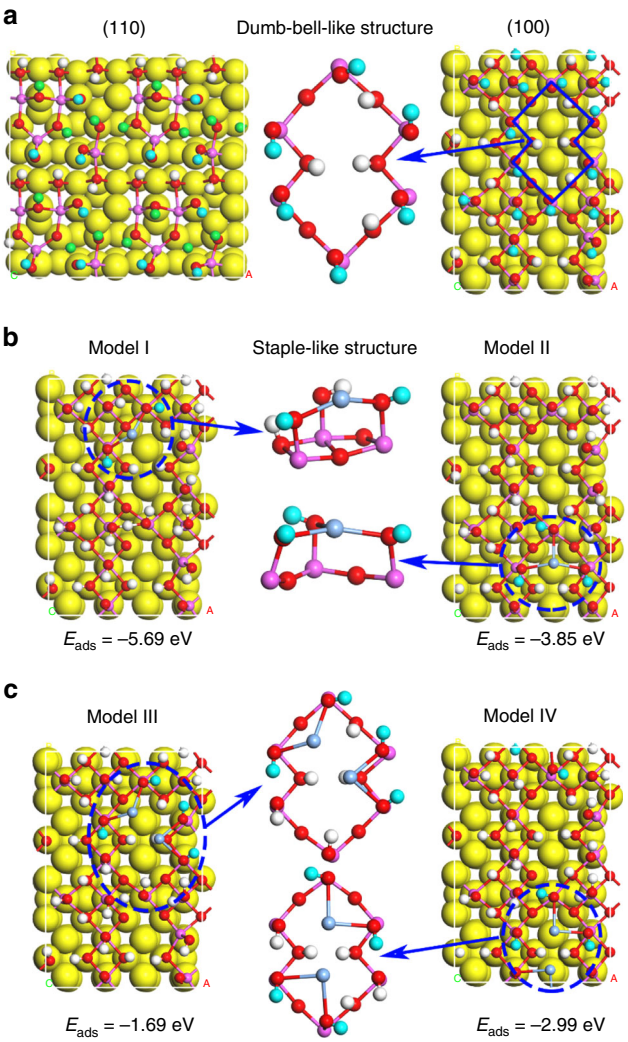

Fig. 5 DFT calculations on interaction between Ag species and hydroxyl groups. a Optimized periodic models of hydroxylation Al_2O_3 (110) surface and Al_2O_3 (100) surface; **b** Optimized periodic models (model I and model II) of the adsorption of Ag atom on (100) surface of Al_2O_3; **c** Optimized periodic models (model III and model IV) of the adsorption of two Ag atoms on (100) surface of Al_2O_3. (pink: Al atom, red: O atom, blue: H atom in terminal hydroxyls (type I), green: H atom in doubly bridging hydroxyls (type II), white: H atom in triply bridging hydroxyls (type III)).

hydroxyls (type II), and one type of triply bridging hydroxyls (type III). The relaxed structure of Ag binding on the hydroxylated (110) surfaces of γ-Al_2O_3 are presented in Supplementary Fig. 6. It is shown that Ag species cannot be stably bonded to any sites, demonstrating that the (110) surface of γ-Al_2O_3 cannot anchor Ag species.

For the (100) surface, only terminal hydroxyls (type I) are on the surface. A stable dumb-bell-like double diamond structure with six terminal hydroxyl groups was formed on the (100) surface (Fig. 5a, blue dotted lines). The relaxed structure of Ag binding on the (100) surfaces of γ-Al_2O_3 is shown in Fig. 5b. Despite the Ag atom is adjacent to O atom of terminal hydroxyls (type I) or triply bridging hydroxyls (type III) in the initial model, the optimized models show that Ag can be only stably bonded to terminal hydroxyls (type I), and a staple-like structure was formed by consuming two or three terminal hydroxyls (type I), producing a new type of doubly bridging hydroxyls (type II′) (consistent with NMR and DRIFTS results shown in Fig. 4). The adsorption energies of Ag in the model I and II are −5.69 and −3.85 eV, respectively, indicating that Ag species are strongly anchored on terminal hydroxyls (type I).

The relaxed structures of second Ag atom binding on the (100) surfaces of γ-Al_2O_3 are shown in Fig. 5c. The second Ag atom was still bonded to terminal hydroxyls (type I), and the adsorption energies of Ag in the model III and model IV are −1.69 and −2.99 eV, respectively. These results indicate that when Ag loading is low and sufficient terminal hydroxyl groups are available, Ag species are mainly anchored on the terminal hydroxyl group sites and easily form a stable single-atom Ag dispersion. However, when Ag loading is high, all terminal hydroxyls are consumed, Ag no longer can be anchored at hydroxyl sites, and it then easily agglomerates and forms metallic Ag cluster during high temperature calcination.

Kwak et al. have suggested that Al^{3+} (Al^{3+}_{penta}) centers are the anchoring sites for Pt species on γ-Al_2O_3[23]. Based on the present results, we propose that Pt anchoring on the γ-Al_2O_3 might be also closely related to the terminal hydroxyl groups rather than Al^{3+}_{penta}. We measured and compared the ^{27}Al MAS NMR signals of nano-Al_2O_3 pretreated with different conditions. The results are presented in Supplementary Fig. 7. When γ-Al_2O_3 was dehydroxylated at 673 K for 12 h, the NMR signal of Al^{3+}_{penta} was clearly detected. However, after the dehydroxylated nano-Al_2O_3 was exposed to ambient air for 12 h, or impregnated in DI-water for 2 h followed by dryness at 378 K for 6 h, the NMR signal of Al^{3+}_{penta} almost disappeared, indicating that Al^{3+}_{penta} sites can be easily coordinatively saturated by interaction with H_2O. These results demonstrate that Al^{3+}_{penta} sites are unlikely available on γ-Al_2O_3 for Ag/Pt anchoring during the catalyst preparation by using impregnation method (in DI-water) whether γ-Al_2O_3 was pretreated or not. We also calculated the adsorption of Ag/Pt atoms on the Al^{3+}_{penta} centers. As shown in Supplementary Figs. 8 and 9, both Ag and Pt atoms can only coordinate with two O atoms adjacent to Al^{3+}_{penta} but not directly with Al^{3+}_{penta} sites. The calculated adsorption energies of Ag/Pt on O atoms adjacent to Al^{3+}_{penta} were also much weaker than the adsorption energies of Ag/Pt on the terminal hydroxyl groups, indicating that both Ag and Pt atoms tend to interact with terminal hydroxyl groups even if the Al^{3+}_{penta} center is available on γ-Al_2O_3. Thus, we believe that the terminal hydroxyl groups are also responsible for the anchoring of Pt on γ-Al_2O_3.

In summary, this comprehensive study reveals that, other than electronic defects and Al^{3+}_{penta} centers, the hydroxyl group is the key site for metal–support interactions that affects the valence state, morphology, and dispersion of Ag species on γ-Al_2O_3. Based on the measurements of MAS NMR, in situ DRIFTS, HAADF-STEM, we show that the Ag species are mainly anchored by the terminal hydroxyl groups (type I) on γ-Al_2O_3 through interaction between Ag and the O atom in Al-OH groups. Nanosized γ-Al_2O_3 entails abundant terminal hydroxyl groups so that Ag could be atomically dispersed on nano-Al_2O_3, while Ag tends to agglomerate to form the Ag clusters on micro-Al_2O_3 since the number of terminal hydroxyl groups are insufficient for Ag binding. Single-atom Ag dispersion on Ag/nano-Al_2O_3 gives rise to markedly higher catalytic performance in HC-SCR of NO, compared with Ag-cluster dispersion. DFT calculations confirm that it is the (100) surfaces of γ-Al_2O_3 that can accommodate much more terminal hydroxyl groups than the (110) surfaces. As such, single Ag atom can be only anchored by the terminal hydroxyls on the (100) surfaces through consuming two or three terminal hydroxyls and forming new doubly bridging hydroxyls. Our study resolves the puzzle on why the single-atom Ag dispersion can be spontaneously achieved only on surface of nanosized γ-Al_2O_3 since nanosized γ-Al_2O_3 entails predominantly the (100) surfaces.

Methods

HAADF-STEM. High-angle annular dark-field scanning transmission electron microscopy (HAADF-STEM) was performed on a Cs-corrected JEOL JEM-ARM 200F operated at 200 kV.

Activity test. The activity test for HC-SCR was performed at steady state in a fixed-bed flow reactor with the gas hourly space velocity (GHSV) of 100,000 h^{-1}. The mixture gas of C_3H_6–H_2-SCR is NO 800 ppm, C_3H_6 1565 ppm, H_2 1%, O_2 10%, and N_2 balance. The mixture gas of ethanol-SCR is NO 800 ppm, C_2H_5OH 1565 ppm, O_2 10%, H_2O 5%, and N_2 balance. An online FTIR spectrometer was used to continuously analyze the concentrations of NO_x.

MAS NMR. ^{27}Al and ^{1}H NMR spectra were recorded at 11.7T on a Bruker-Advance^{III} 500 spectrometer equipped with a 4 mm double-resonance probe. The corresponding resonance frequency and magic angle spinning rate were 500.57 MHz and 10 kHz respectively. ^{27}Al NMR measurements were conducted with no pretreatment on the samples. For ^{1}H NMR measurements, samples were pre-dehydrated on a vacuum line. The temperature was gradually increased at a rate of 1 K min^{-1} and the sample was kept at a final temperature of 473 K and at a pressure below 10^{-3} Pa for 12 h. The average weight of samples is 0.0513 g and the deviation for samples is lower than 2.7%, all NMR spectra were normalized to the sample weight.

XAFS. Ag K-edge XAFS spectra were recorded in transmission mode at room temperature, using the BL14W1 XAFS beam line at the Shanghai Synchrotron Radiation Facility. The XANES and EXAFS data reduction and analysis were performed using the Athena program that is part of the IFFEFIT software package[62,63]. The filtered k^2 weighted $\chi(k)$ was Fourier-transformed into R space (k range: 2.9–14.3 $Å^{-1}$ for Ag-K EXAFS).

In situ DRIFTS. The in situ diffuse reflectance infrared Fourier transform spectroscopy (DRIFTS) was conducted on a Nexus 670 (Thermo Nicolet) FTIR equipped with an MCT/A detector. All spectra were recorded in the range 4000–800 cm^{-1} by accumulating 100 scans with a resolution of 4 cm^{-1}. A background spectrum was subtracted from each spectrum. Samples were pretreated at 473 K for 30 min in a flow of $N_2 + O_2$ (20%) before in situ DRIFTS measurements.

DFT calculations. Geometries and energies were calculated using the DFT method in the formalism of Perdew–Burke–Ernzerhof (PBE) functional[64] with van der Waals correction proposed by Becke-Jonson (i.e., DFT-D3 method)[65], as implemented in the Vienna ab initio simulation package (VASP 5.4.4)[66]. The projector augmented wave method was used to describe the interaction between the ions and the electrons[67]. Convergence tests were performed for all initial parameters. The vacuum gap was 20 Å so that inter-slab interactions were negligible in the periodic systems. DFT calculations were carried out with a plane-wave energy cutoff of 400 eV. Based on our previous reports[68,69], the dehydrated (110) and (100) surfaces of γ-Al_2O_3 were modeled using (2 × 2) supercells. According to our preliminary convergence test, Monkhorst−Pack k-point sets of (1 × 1 × 1) were used for the Al_2O_3 surfaces. The top two layers and the adsorbents were fully relaxed, while the bottom layers were fixed to mimic the bulk region. The adsorption energies of Ag/Pt on the γ-Al_2O_3 surface were calculated as follows: $E_{ad} = E_{adsorbate+surface} - (E_{surface} + E_{adsorbate})$, where $E_{adsorbate+surface}$ and $E_{surface}$ are the total energies of the adsorbed system and alumina slab, respectively; and E_{ad} reflects the stability of the adsorbates on the γ-Al_2O_3 surface. Negative E_{ad} values mean that the adsorbed state is energetically favorable. The DFT-predicted adsorption energies of Ag/Pt

atom are with respect to the energy of a gas-phase Ag atom. All the DFT computations were spin polarized. We compute the adsorption energy of Ag on the γ-Al_2O_3 (110) surface, with (−5.76 eV) and without dipole correction (−5.69 eV). The difference in the adsorption energy of Ag is less than 1.2%. Consequently, all calculation results do not include the dipole correction.

Data availability

The authors declare that the data supporting the findings of this study are available within the paper and its supplementary information files. All relevant data are available from the correspondence authors upon reasonable request.

Received: 15 August 2019; Accepted: 9 December 2019;
Published online: 27 January 2020

References

1. Deng, H. et al. Nature of Ag species on Ag/γ-Al_2O_3: a combined experimental and theoretical study. *ACS Catal.* **4**, 2776–2784 (2014).
2. Bethke, K. A. & Kung, H. H. Supported Ag catalysts for the lean reduction of NO with C_3H_6. *J. Catal.* **172**, 93–102 (1997).
3. Chaieb, T. et al. Insights into the influence of the Ag loading on Al_2O_3 in the H_2-assisted C_3H_6-SCR of NOx. *Appl. Catal. B* **156–157**, 192–201 (2014).
4. Yu, Y., He, H. & Feng, Q. Novel enolic surface species formed during partial oxidation of CH_3CHO, C_2H_5OH, and C_3H_6 on Ag/Al_2O_3: An in situ DRIFTS study. *J. Phys. Chem. B* **107**, 13090–13092 (2003).
5. Yu, Y., He, H., Feng, Q., Gao, H. & Yang, X. Mechanism of the selective catalytic reduction of NOx by C_2H_5OH over Ag/Al_2O_3. *Appl. Catal. B* **49**, 159–171 (2004).
6. Kim, P. S., Kim, M. K., Cho, B. K., Nam, I.-S. & Oh, S. H. Effect of H_2 on deNOx performance of HC-SCR over Ag/Al_2O_3: morphological, chemical, and kinetic changes. *J. Catal.* **301**, 65–76 (2013).
7. Shimizu, K.-i & Satsuma, A. Reaction mechanism of H_2-promoted selective catalytic reduction of NO with NH_3 over Ag/Al_2O_3. *J. Phys. Chem. C.* **111**, 2259–2264 (2007).
8. Fogel, S., Doronkin, D. E., Gabrielsson, P. & Dahl, S. Optimisation of Ag loading and alumina characteristics to give sulphur-tolerant Ag/Al_2O_3 catalyst for H_2-assisted NH_3-SCR of NOx. *Appl. Catal. B* **125**, 457–464 (2012).
9. Villani, K., Brosius, R. & Martens, J. A. Catalytic carbon oxidation over Ag/Al_2O_3. *J. Catal.* **236**, 172–175 (2005).
10. Gao, Y. et al. Aggregation and redispersion of silver species on alumina and sulphated alumina supports for soot oxidation. *Catal. Sci. Technol.* **7**, 3524–3530 (2017).
11. Zhang, L., Zhang, C. & He, H. The role of silver species on Ag/Al_2O_3 catalysts for the selective catalytic oxidation of ammonia to nitrogen. *J. Catal.* **261**, 101–109 (2009).
12. Wang, F. et al. Nanosize effect of Al_2O_3 in Ag/Al_2O_3 catalyst for the selective catalytic oxidation of ammonia. *ACS Catal.* **8**, 2670–2682 (2018).
13. Gang, L., Anderson, B. G., van Grondelle, J. & van Santen, R. A. Low temperature selective oxidation of ammonia to nitrogen on silver-based catalysts. *Appl. Catal. B* **40**, 101–110 (2003).
14. Li, Y. et al. Effect of the pressure on the catalytic oxidation of volatile organic compounds over Ag/Al_2O_3 catalyst. *Appl. Catal. B* **89**, 659–664 (2009).
15. Cordi, E. M. & Falconer, J. L. Oxidation of volatile organic compounds on a Ag/Al_2O_3 catalyst. *Appl. Catal. A* **151**, 179–191 (1997).
16. Mark Ormerod, R., Peat, K. L., Wytenburg, W. J. & Lambert, R. M. Electron spectroscopic investigation of ultra-selective ethylene epoxidation: studies with Ag(111) and (110) model systems and with Ag/Al_2O_3 catalysts. *Surf. Sci.* **269–270**, 506–513 (1992).
17. Boskovic, G., Dropka, N., Wolf, D., Brückner, A. & Baerns, M. Deactivation kinetics of Ag/Al_2O_3 catalyst for ethylene epoxidation. *J. Catal.* **226**, 334–342 (2004).
18. Tauster, S. J., Fung, S. C. & Garten, R. L. Strong metal-support interactions. Group 8 noble metals supported on TiO_2. *J. Am. Chem. Soc.* **100**, 170–175 (1978).
19. Tauster, S. J., Fung, S. C., Baker, R. T. K. & Horsley, J. A. Strong interactions in supported-metal catalysts. *Science* **211**, 1121–1125 (1981).
20. Li, Y. et al. High temperature reduction dramatically promotes Pd/TiO_2 catalyst for ambient formaldehyde oxidation. *Appl. Catal. B* **217**, 560–569 (2017).
21. Chen, M. S. & Goodman, D. W. The structure of catalytically active gold on titania. *Science* **306**, 252–255 (2004).
22. Lopez, N. et al. The adhesion and shape of nanosized Au particles in a Au/TiO_2 catalyst. *J. Catal.* **225**, 86–94 (2004).
23. Kwak, J. H. et al. Coordinatively unsaturated Al^{3+} centers as binding sites for active catalyst phases of platinum on γ-Al_2O_3. *Science* **325**, 1670–1673 (2009).
24. Jacobsen, C. J. H., Topsøe, N. Y., Topsøe, H., Kellberg, L. & Jakobsen, H. J. Quantitative ^{1}H MAS NMR studies of structurally different OH surface groups on η-Al_2O_3 and Mo/η-Al_2O_3 catalysts. *J. Catal.* **154**, 65–68 (1995).
25. Dutov, V. V. et al. Low-temperature CO voxidation over Ag/SiO_2 catalysts: effect of OH/Ag ratio. *Appl. Catal. B* **221**, 598–609 (2018).
26. Pasricha, R., Gupta, S. & Srivastava, A. K. A facile and novel synthesis of Ag-graphene-based nanocomposites. *Small* **5**, 2253–2259 (2009).
27. Zhang, Z. et al. Tubular nanocomposite catalysts based on size-controlled and highly dispersed silver nanoparticles assembled on electrospun silicananotubes for catalytic reduction of 4-nitrophenol. *J. Mater. Chem.* **22**, 1387–1395 (2012).
28. Hu, X., Zhu, Q., Wang, X., Kawazoe, N. & Yang, Y. Nonmetal–metal–semiconductor-promoted P/Ag/Ag_2O/Ag_3PO_4/TiO_2 photocatalyst with superior photocatalytic activity and stability. *J. Mater. Chem. A* **3**, 17858–17865 (2015).
29. Xu, G., Ma, J., He, G., Yu, Y. & He, H. An alumina-supported silver catalyst with high water tolerance for H_2 assisted C_3H_6-SCR of NOx. *Appl. Catal. B* **207**, 60–71 (2017).
30. Shibata, J. et al. Structure of active Ag clusters in Ag zeolites for SCR of NO by propane in the presence of hydrogen. *J. Catal.* **227**, 367–374 (2004).
31. Shimizu, K.-i et al. Reductive activation of O_2 with H_2-reduced silver clusters as a key step in the H_2-promoted selective catalytic reduction of NO with C_3H_8 over Ag/Al_2O_3. *J. Phys. Chem. C* **111**, 950–959 (2007).
32. Gachard, E., Belloni, J. & Subramanian, M. A. Optical and EPR spectroscopic studies of silver clusters in Ag, Na-Y zeolite by γ-irradiation. *J. Mater. Chem.* **6**, 867–870 (1996).
33. Arvea, K. et al. Preparation and characterisation of Agalumina catalysts for the removal of NOx emissions under oxygen rich conditions. *Top. Catal.* **30/31**, 91–95 (2004).
34. Keshavaraja, A., She, X. & Flytzani-Stephanopoulos, M. Selective catalytic reduction of NO with methane over Ag-alumina catalysts. *Appl. Catal. B* **27**, L1–L9 (2000).
35. Hu, C. et al. Plasmon-induced photodegradation of toxic pollutants with Ag-AgI/Al_2O_3 under visible-light irradiation. *J. Am. Chem. Soc.* **9**, 857–862 (2009).
36. Kung, K. A. B. A. H. H. Supported Ag catalysts for the lean reduction of NO with C_3H_6. *J. Catal.* **172**, 93–102 (1997).
37. Ken-ichi, S. et al. Silver-alumina catalysts for selective reduction of NO by higher hydrocarbons: structure of active sites and reaction mechanism. *Appl. Catal. B* **30**, 151–162 (2001).
38. Sandoval, A., Aguilar, A., Louis, C., Traverse, A. & Zanella, R. Bimetallic Au–Ag/TiO_2 catalyst prepared by deposition–precipitation: high activity and stability in CO oxidation. *J. Catal.* **281**, 40–49 (2011).
39. Nagai, Y. et al. Sintering inhibition mechanism of platinum supported on ceria-based oxide and Pt-oxide–support interaction. *J. Catal.* **242**, 103–109 (2006).
40. Verma, P., Yuan, K., Kuwahara, Y., Mori, K. & Yamashita, H. Enhancement of plasmonic activity by Pt/Ag bimetallic nanocatalyst supported on mesoporous silica in the hydrogen production from hydrogen storage material. *Appl. Catal. B* **223**, 10–15 (2018).
41. Zhou, W. et al. Composites of small Ag clusters confined in the channels of well-ordered mesoporous anatase TiO_2 and their excellent solar-light-driven photocatalytic performance. *Nano Res.* **7**, 731–742 (2014).
42. Sherry, H. S. The ion-exchange properties of zeolites. I. Univalent ion exchange in synthetic Faujasite. *J. Phys. Chem.* **70**, 1158–1168 (1966).
43. Taoufik, M. et al. Heteronuclear NMR spectroscopy as a surface-selective technique: a unique look at the hydroxyl groups of gamma-alumina. *Chem. Eur. J.* **20**, 4038–4046 (2014).
44. Li, W. et al. Probing the surface of gamma-Al_2O_3 by oxygen-17 dynamic nuclear polarization enhanced solid-state NMR spectroscopy. *Phys. Chem. Chem. Phys.* **20**, 17218–17225 (2018).
45. Zhang, F. et al. Enhanced metathesis activity and stability of methyltrioxorhenium on a mostly amorphous alumina: Role of the local grafting environment. *J. Am. Chem. Soc.* **140**, 13854–13868 (2018).
46. Barrow, B. N. S., Scullard, A. & Collis, N. Surface selective ^{1}H and ^{27}Al MAS NMR observations of strontium oxide doped alumina. *Johns. Matthey Technol. Rev.* **60**, 90–97 (2016).
47. Ramis, G., Yi, L. & Busca, G. Ammonia activation over catalysts for the selective catalytic reduction of NO_x and the selective catalytic oxidation of NH_3. An FT-IR study. *Catal. Today* **28**, 373–380 (1996).
48. Long, R. Q. & Yang, R. T. Selective catalytic reduction of nitrogen oxides by ammonia over Fe^{3+}-exchanged TiO_2-pillared clay catalysts. *J. Catal.* **186**, 254–268 (1999).
49. Topsrae, N.-Y. Mechanism of the selective catalytic reduction of nitric oxide by ammonia elucidated by in situ on-line fourier transform infrared spectroscopy. *Science* **265**, 1217–1219 (1994).

50. Amores, J. M. G., Escribano, V. S., Ramis, G. & Busca, G. An FT-IR study of ammonia adsorption and oxidation over anatase-supported metal oxides. *Appl. Catal. B* **13**, 45–58 (1997).
51. Zhang, L. & He, H. Mechanism of selective catalytic oxidation of ammonia to nitrogen over Ag/Al_2O_3. *J. Catal.* **268**, 18–25 (2009).
52. Cornac, M., Janin, A. & Lavalley, J. C. Application of FTIR spectroscopy to the study of sulfidation of Mo catalysts supported on alumina or silica (4000–400 cm^{-1} range). *Infrared Phys. Technol.* **24**, 143–150 (1984).
53. Zaki, M. I. & Knözinger, H. Carbon monoxide—a low temperature infrared probe for the characterization of hydroxyl group properties on metal oxide surfaces. *Mater. Chem. Phys.* **17**, 201–215 (1987).
54. Wagner, G. W. et al. Reactions of VX, GB, GD, and HD with nanosize Al_2O_3. Formation of aluminophosphonates. *J. Am. Chem. Soc.* **123**, 1636–1644 (2001).
55. DeCanio, E. C. et al. Solid-State ^1H MAS NMR characterization of γ-alumina and modified γ-Aluminas. *J. Catal.* **148**, 76–83 (1994).
56. Knözinger, H. et al. Catalytic aluminas: surface models and characterization of surface sites. *Catal. Rev.* **17**, 31–70 (1978).
57. Nortier, P. et al. Effects of crystallinity and morphology on the surface properties ofalumina. *Appl. Catal.* **61**, 141–160 (1990).
58. Ballinger, T. H. et al. IR spectroscopic detection of Lewis acid sites on Al_2O_3 using adsorbed CO. Correlation with Al-OH group removal. *Langmuir* **7**, 3041–3045 (1991).
59. Choong, C. K. S. et al. Effect of calcium addition on catalytic ethanol steam reforming of Ni/Al_2O_3: I. Catalytic stability, electronic properties and coking mechanism. *Appl. Catal. A* **407**, 145–154 (2011).
60. Puurunen, R. L. et al. Successive reactions of gaseous trimethylaluminium and ammonia on porous alumina. *Phys. Chem. Chem. Phys.* **3**, 1093–1102 (2001).
61. Digne, M. et al. Hydroxyl groups on γ-alumina surfaces: a DFT study. *J. Catal.* **211**, 1–5 (2002).
62. Newville, M. IFEFFIT: interactive XAFS analysis and FEFF fitting. *J. Synchrotron Radiat.* **8**, 322–324 (2001).
63. Ravel, B. et al. ATHENA, ARTEMIS, HEPHAESTUS: data analysis for X-ray absorption spectroscopy using IFEFFIT. *J. Synchrotron Radiat.* **12**, 537–541 (2005).
64. Perdew, J. P. et al. Generalized gradient approximation made simple. *Phys. Rev. Lett.* **77**, 3865–3868 (1996).
65. Grimme, S., Ehrlich, S. & Goerigk, L. Effect of the damping function in dispersion corrected density functional theory. *J. Comput. Chem.* **32**, 1456–1465 (2011).
66. Kresse, G. & Furthmüller, J. Efficient iterative schemes for ab initio total-energy calculations using a plane-wave basis set. *Phys. Rev. B* **54**, 11169–11186 (1996).
67. Kresse, G. & Joubert, D. From ultrasoft pseudopotentials to the projector augmented-wave method. *Phys. Rev. B* **59**, 1758–1775 (1999).
68. Deng, H., Yu, Y. & He, H. Adsorption states of typical intermediates on Ag/Al_2O_3 catalyst employed in the selective catalytic reduction of NOx by ethanol. *Chin. J. Catal.* **36**, 1312–1320 (2015).
69. Deng, H., Yu, Y. & He, H. Discerning the role of Ag–O–Al entities on $Ag/\gamma\text{-}Al_2O_3$ surface in NO_x selective reduction by ethanol. *J. Phys. Chem. C* **119**, 3132–3142 (2015).

Acknowledgements

CZ team is supported by the National Key R&D Program of China (2017YFC0211802, 2017YFC0211101, 2016YFC0207104), the National Natural Science Foundation of China (21577159, 21876191) and the Youth Innovation Promotion Association, CAS (2017064). XCZ is supported by University of Nebraska-Lincoln Holland Computing Center.

Author contributions

F.W. carried out the sample preparation as well as the XAFS, in situ DRIFTS, MAS NMR and HAADF-STEM experiments, and assisted with writing the manuscript. J.M. carried out the DFT calculations and assisted with writing the manuscript. S.X., Q.W., and J.X. carried out the NMR experiments. C.Z. oversaw and directed the study and assisted with writing the manuscript. X.C.Z. assisted with DFT calculations, interpretation of experimental results, and writing the manuscript. H.H. conceived the project and assisted with writing the manuscript.

Competing interests

The authors declare no competing interests.

Additional information

Supplementary information is available for this paper at https://doi.org/10.1038/s41467-019-13937-1.

Correspondence and requests for materials should be addressed to C.Z. or X.C.Z.

Peer review information *Nature Communications* thanks Cyril Thomas and the other anonymous reviewers for their contribution to the peer review of this work.

Reprints and permission information is available at http://www.nature.com/reprints

Publisher's note Springer Nature remains neutral with regard to jurisdictional claims in published maps and institutional affiliations.